Full length article

Origin of the yield stress anomaly in L1$_2$ intermetallics unveiled with physically informed machine-learning potentials

Xiang Xu [a,b,*], Xi Zhang [a,*], Erik Bitzek [c], Siegfried Schmauder [b], Blazej Grabowski [a]

[a] *Institute for Materials Science, University of Stuttgart, Pfaffenwaldring 55, 70569 Stuttgart, Germany*
[b] *Institute for Materials Testing, Materials Science and Strength of Materials, University of Stuttgart, Pfaffenwaldring 32, 70569 Stuttgart, Germany*
[c] *Computational Materials Design, Max Planck Institute for Sustainable Materials, Max–Planck-Straße 1, 40237, Düsseldorf, Germany*

ARTICLE INFO

ABSTRACT

The yield stress anomaly of L1$_2$ intermetallics such as Ni$_3$Al, Ni$_3$Ga, Co$_3$(Al,W) is controlled by the so-called Kear–Wilsdorf lock (KWL), of which the formation and unlocking are governed by dislocation cross-slip. Despite the importance of this anomalous behavior in L1$_2$-strengthened alloys, microscopic understanding of the KWL is limited. Here, molecular dynamics simulations are conducted by employing a dedicated machine-learning interatomic potential derived via physically informed active learning. The potential facilitates modeling of the dislocation behavior in Ni$_3$Al with near *ab initio* accuracy. KWL formation and unlocking are observed and analyzed. The unlocking stress demonstrates a pronounced temperature dependence, contradicting the assumptions of existing analytical models. A phenomenological model is proposed to effectively describe the atomistic unlocking stresses and extrapolate them to the macroscopic scale. The model is general and applicable to other L1$_2$ intermetallics. The acquired knowledge of KWLs provides a deeper understanding on the origin of the yield stress anomaly.

1. Introduction

Ni-based superalloys are used for turbine blades because they withstand thermal mechanical loading under high turbine-entry temperatures [1,2]. Over several generations of these superalloys and corresponding thermal barrier coatings, the turbine-entry temperatures have increased by 700 K [3], significantly improving the thermodynamic efficiency of aircraft engines. The outstanding thermal resistance mainly originates from a high volume fraction of L1$_2$-ordered precipitates. In contrast to common structural materials, the yield stress of certain L1$_2$ intermetallics, e.g., Ni$_3$Al [4], Ni$_3$Ga [5], or Co$_3$(Al,W) [6], increases with temperature, typically accompanied with an anomalously increasing work-hardening rate. As this so-called yield stress anomaly (YSA) is pivotal for strengthening advanced alloys, the steady increase of understanding YSA has been a key ingredient to the evolution of Ni-based superalloys [1,2,7] and Co-based superalloys [8–10], and also for the development of L1$_2$ strengthened high-entropy alloys [11,12].

However, the origin of YSA is still not satisfactorily clarified [7]. What is known from transmission electron microscopy (TEM) on samples deformed in the temperature region of the YSA [13,14] is that the dislocations in Ni$_3$Al exhibit a unique non-planar dislocation core structure—nowadays referred to as the Kear–Wilsdorf lock (KWL). The dislocation core was shown to evolve through cross-slip [15,16] in

which three planar defects are involved: two antiphase boundaries (APBs) on the (100) and (111) planes plus a complex stacking fault (CSF).

Several analytical models [17–23] have been proposed to comprehend KWLs and their relation to YSA, considering factors like the difference between the formation energies of the (111)APB and (100)APB [17], and torque interactions between the superpartials [18]. The "APB-jump" phenomenon observed in *in situ* TEM experiments [15] brought forward a model based on the competition between the formation and unlocking of the incomplete KWL [20]. An incomplete KWL is built up from APBs on both the (100) and (111) planes, while a complete KWL contains only an APB on the (100) plane (see Figure S1 in Supplementary Material). A common limitation of existing models is the assumption of an athermal unlocking process [20,22].

Despite the importance of KWLs, the understanding of their formation and unlocking is limited, especially regarding the atomistic evolution during cross-slip. A close atomistic inspection is difficult with experiments but becomes feasible with atomistic simulations. For example, the embedded atom method (EAM) has been used to investigate the dissociation of superdislocation in Ni$_3$Al [24,25], to calculate the nucleation energy of the cross-slip process for a single dislocation [26,27] and for intersecting dislocations [28]. These

---

* Corresponding authors.
  E-mail addresses: xiang.xu@imw.uni-stuttgart.de (X. Xu), xi.zhang@imw.uni-stuttgart.de (X. Zhang).

simulation studies focused on energetics at 0 K and thus neglected entropy contributions relevant at elevated temperatures. Recently, the temperature-dependent dislocation dynamics of an edge dislocation in Ni_3Al has been investigated using EAM potential [29]. However, atomistic simulations for the behavior of screw superdislocations, particularly when related to KWLs and cross-slip processes at elevated temperatures, are still absent. This is presumably due to the limited accuracy of existing potentials in predicting the energetics of planar defects, which prevents the occurrence of dislocation cross-slip.

In the present study, a machine-learning interatomic potential (MLIP), specifically a Moment Tensor Potential (MTP) [30,31], is developed and utilized to simulate the dislocation activity in Ni_3Al at near *ab initio* accuracy and with the inclusion of finite temperature effects. The most critical aspect in designing MLIPs is the proper choice of the fitting dataset from density functional theory (DFT). To guarantee an accurate description of the dislocation, we utilize a physically informed active-learning scheme and evaluate the MLIP specifically on the temperature dependence of the planar defect energies. The MLIP enables the study of the unlocking of KWLs by shearing at different temperatures in molecular dynamics (MD) simulations. Based on the obtained data, a phenomenological model for *thermally* activated KWL unlocking is derived.

2. Methods

2.1. Moment tensor potential

The moment descriptor $M_{\mu,\nu}$ in the MTP formalism describes atomic interactions with both radial and angular information according to [30]

$$M_{\mu,\nu} = \sum_j f_\mu(|\vec{r}_{ij}|, z_i, z_j) \underbrace{\vec{r}_{ij} \otimes \cdots \otimes \vec{r}_{ij}}_{\nu \text{ times}}, \tag{1}$$

in which $f_\mu(|\vec{r}_{ij}|, z_i, z_j)$ is the radial function for particle i (type z_i at $\vec{r}_i$) interacting with its neighbor j (type z_j at $\vec{r}_j$); μ stands for the number of radial functions (depending on the level of the contraction introduced next); $\vec{r}_{ij} \otimes \cdots \otimes \vec{r}_{ij}$ is a tensor of rank ν representing the angular interaction ($\otimes$ denotes the outer product). The scalar contractions of the moments $M_{\mu,\nu}$ give the basis functions B_α. With these basis functions, the local interatomic potential $V(\mathfrak{n}_i)$ for atom i with its environment $\mathfrak{n}_i$ is linearly expanded as

$$V(\mathfrak{n}_i) = \sum_\alpha \xi_\alpha B_\alpha(\mathfrak{n}_i), \tag{2}$$

and the energy of the system is then obtained by

$$E^{\text{MTP}} = \sum_i V(\mathfrak{n}_i). \tag{3}$$

In practice, the number of basis functions is restricted by a degree-like measure, the maximum level lev_{max}, and, further, atomic interactions beyond a cutoff radius R_{cut} are neglected. To maintain high accuracy at a computationally reasonable number of hyperparameters, a level of $\text{lev}_{\text{max}} = 12$ and a cutoff radius of $R_{\text{cut}} = 5$ Å were chosen. The weights of the energy and force contributions in the calculation of the loss function were set equal to 1.0, 0.01 Å^2, respectively, while stresses were not considered for training.

Ab initio molecular dynamics (AIMD) entering the MTP fitting dataset was performed for all investigated structures at six different volumes at 1600 K. This temperature was chosen to ensure that the trained MTP can capture the high-temperature behavior, particularly the significant anharmonicity of the planar defects near the melting point [32,33]. The configurations from the AIMD for each structure served as preliminary information for training the MTP in the corresponding active-learning (AL) loop.

The workflow for training the MTPs contains multi AL-loops and will be elaborated in Section 3.1. Each AL-loop includes four steps: (1) get/train an MTP; (2) perform MD simulations with this MTP to select new configurations; (3) perform DFT calculations for selected configurations and (4) go to step (1). (For a detailed introduction, see Ref. [31].) MTP MD simulations were run for 10 picoseconds with the Langevin thermostat at a timestep of 1 femtosecond. MD snapshots were evaluated by calculating the extrapolation grade γ_{mv} according to the maxvol algorithm [31,34]. The threshold to break an MD simulation was set to $\gamma_{\text{mv}}^{\text{break}} = 3.0$ and the selection threshold to $\gamma_{\text{mv}}^{\text{select}} = 1.5$. An AL-loop was finished if no configuration got selected in step (2), meaning that γ_{mv} for all MD snapshots was below 1.5. As an exception, the AL-loop for the surface structures was run until the extrapolation grade was below 3.0. This is sufficient for the surface structures since they are needed only for the free boundary conditions of the shearing simulations, and they have negligible influence on the dislocation behavior.

2.2. Density-functional-theory calculations

The DFT calculations were performed by using VASP [35,36] with potentials based on the projector augmented wave (PAW) method [37] and within the PBE-GGA approximation [38] to the exchange–correlation functional. A plane wave cutoff energy of 400 eV was used. Regarding the magnetic contribution, which was concluded to have a significant influence on the formation energy of planar defects in particular for the (100)APB [32], spin-polarization was considered in all the DFT calculations. An MTP trained with a spin-unpolarized dataset was tested, and the related discussion is provided in the Supplementary Material (Section S6).

2.3. Free energy calculations

The Gibbs energy $G(T)$ was obtained via the Legendre transformation of the Helmholtz free energy $F(T)$, which was computed according to

$$F(T) = E_{0K} + F^{\text{qh}}(T) + F^{\text{ah}}(T), \tag{4}$$

with the total energy at zero-Kelvin E_{0K}, the quasiharmonic contribution $F^{\text{qh}}(T)$, and the anharmonic contribution $F^{\text{ah}}(T)$. While F^{qh} was calculated by using the finite displacement method (pre- and post-processing performed with Phonopy [39]), F^{ah} was obtained by using thermodynamic integration from the quasiharmonic reference to the full vibrational state,

$$F^{\text{ah}} = \int_0^1 d\lambda \langle E^{\text{vib}} - E^{\text{qh}} \rangle_\lambda, \tag{5}$$

with λ the coupling factor between the full vibrational state with energy E^{vib} and the qh-reference with energy E^{qh}.

The Gibbs formation energy of the planar defects was then obtained as

$$\Delta G_{\text{form}}(T) = \frac{G_{\text{defect}}(T) - G_{\text{bulk}}(T)}{A_{\text{defect}}(T)}, \tag{6}$$

with the Gibbs energies G_{defect} and G_{bulk} of the planar defect and bulk supercell, respectively, and with the area of the planar defect A_{defect}.

2.4. Molecular dynamics simulations

ATOMSK [40] was used to generate the initial dislocation configuration according to dislocation theory [41]. Specifically, two $1/2 \langle 1\bar{1}0 \rangle$ screw superpartials were inserted into the model, bound with a (111)APB region, as shown in Figure S2(a). During relaxation, each superpartial dissociated into two Shockley partials, generating a CSF ribbon in between. The dislocation model was made of 1.5 million atoms with dimensions of 20.3 nm, 35.1 nm, and 24.8 nm along the x, y, and z-axis, respectively. The dislocation line as well as the Burger's vector were placed parallel to the x-axis. Periodic boundary conditions were applied along the x- and y-direction, while the boundary conditions along the z-direction were shrink-wrapped.

MTP MD simulations were performed with LAMMPS [42]. To generate an incomplete KWL, the model was first equilibrated at a higher temperature, e.g., 1000 K, to ensure the activation of the cross-slip process within a reasonable simulation time frame. An incomplete KWL with a cross-slip distance of $w = 2\delta$ (δ: the distance between the two nearest atomic planes along the [111] direction) was selected, quenched to 400 K, and then fully equilibrated at zero pressure. Before the shearing simulations, three statistical samples initiated with different velocities were heated up to the target temperature in 10 ps and then fully equilibrated for 20 ps. All the MD simulations were performed with a timestep of 0.001 ps.

For the shearing simulations, atoms located within a thickness of 9 atomic planes ($\approx$1.9 nm) on the top and bottom of the box were selected to apply the shear (brown regions in Figure S2(a)). These atoms were treated with flexible boundary conditions to avoid spurious forces on the dislocation [43]. The shearing direction was set along the *x*-axis (parallel to the Burger's vector), such that the core of the dislocation was moving along the *y*-axis.

The shearing simulations to unlock the incomplete KWL were performed at a set of strain rates $\dot{\gamma} = 1 \times 10^{-5}$, 5×10^{-6}, 2×10^{-6} ps^{-1} and temperatures $T = 650, 700, 800, 850, 900, 950, 1000, 1050, 1100$ K. Test simulations were also performed with $\dot{\gamma}$ of 1×10^{-6} ps^{-1}. For each temperature, samples were pre-sheared with $\dot{\gamma} = 1 \times 10^{-4}$ ps^{-1} to a pre-strain γ_0. Then, the production calculations were restarted by continuing shearing from the point of γ_0 with the same atomic state, i.e., atomic positions, velocities, and forces. The pre-strain γ_0 was selected such that there was enough time (more than 100 ps) for equilibration before the occurrence of the first cross-slip, e.g., $\gamma_0 = 0.5\%$ for simulations with $\dot{\gamma} = 1 \times 10^{-5}$, 5×10^{-6} ps^{-1}. A larger γ_0 was used in the shearing simulations with $\dot{\gamma} = 2 \times 10^{-6}$ ps^{-1}, to make sure that unlocking is possible within a reasonable computational time (10 ns). Such treatment does not only increase the efficiency of the calculations but also maintains the desired core structure (as illustrated in Figure S2(c)) for high-temperature simulations, e.g., at 1000 K. Note that utilizing a high accuracy MTP and performing shearing at a rate of 2×10^{-6} ps^{-1} (or even slower at 1×10^{-6} ps^{-1}) for models containing more than one million atoms touches the limits of typical computational resources. For example, to unlock the KWL at a shear rate of 2×10^{-6} ps^{-1} two nanoseconds of simulation time are required amounting to 2 million MD steps (excluding the pre-straining). Such a calculation took 23.5 h of real-time on 2560 cores (AMD EPYC 7742, 2.25 GHz), summing up to 60 160 core hours.

3. Results

3.1. Physically informed active-learning

Active-learning [31] has been successfully used in different machine-learning studies [44,45]. However, for the present purpose, the standard AL scheme cannot be applied due to the large, DFT-inaccessible supercell size required to model a KWL (>1 million of atoms). Hence, we devise a modified AL scheme, in the spirit of two very recent schemes applied to large-scale silicon–oxygen systems [46] and to dissociated partial dislocations [47]. The key idea is to decompose the KWL into its physically relevant parts, which *can* be modeled with (periodic) DFT. The choice of the relevant parts is guided by domain expertise and is displayed in Fig. 1(a). Besides the perfect bulk, which is clearly required as the basic fitting input, we know that a KWL is formed by the (100)APB, the (111)APB, and the CSF. For the present shearing simulations, we also need the (111) surface due to the boundary conditions. Additionally, we include the superlattice intrinsic stacking fault (SISF), and Al and Ni vacancies into the fitting dataset, in case they should form at high temperatures. Note that the present dataset also enables a broader applicability of the MLIP, for example, for investigations of creep properties.

For each such geometry a usual AL is performed at a high temperature (here 1600 K). The different AL steps are executed successively in a row. We start with the perfect bulk AL and take the resulting MTP as input to the next AL step for the (100)APB. This process continues for the remaining geometries until a final MTP is obtained. The sequence is displayed in Fig. 1(a). Fitting the MTP in such a systematic way allows us to monitor the accuracy at each step. As usual, one measure of the MTP accuracy is the root mean square error (RMSE) in energies and forces. The force RMSE stays almost unchanged while the energy RMSE increases by a factor of 2.4 during the AL steps (cf. Fig. 1(a)). The final training errors of 1.59 meV/atom and 0.056 eV/Å are small, considering the high temperature and structural complexity of the fitting dataset.

An additional measure that we employ here and that gives us control over the accuracy in describing the geometry of interest, i.e., the KWL, is the locally resolved extrapolation grade. The extrapolation grade is a metric that quantifies how far away a certain atomic configuration is located in phase space with respect to the fitting dataset.[1] The advantage is that no extra DFT calculation is required and thus the grade can be computed for the target geometry even if a large supercell is required, as for the KWL. Specifically, we utilize our final MTP to generate KWL snapshots for which we resolve the extrapolation grade locally. We do this for the different MTPs obtained from our physically informed AL scheme and investigate how the grade changes along the sequence of AL steps (Supplement Figure S4). The MTP trained with bulk structures only (MTP-bulk) describes the perfect bulk atoms (i.e., 98.8% of all atoms) with a grade of ≲1, which indicates an interpolative behavior. Atoms belonging to the KWL are revealed to have a slightly higher grade which indicates an extrapolative behavior. Upon inclusion of the (100)APB and (111)APB geometries into the physically informed AL, the extrapolation grade steadily improves, reaching a grade of ≲1 also in the KWL region. The analysis of the local grade thus gives increased confidence in the predictive capability of the MTP in the most relevant simulation region.

As a further quality measure, the final MTP is evaluated on the free energy surfaces for bulk Ni$_3$Al, the APBs, and the CSF, up to the melting point 1668 K. The thermal properties of perfect bulk Ni$_3$Al are well predicted by the MTP over a large temperature range (Figure S5 in the Supplementary Material). The resulting temperature-dependent planar defect energies (red curves in Fig. 1 from (b)–(d)) are likewise in good agreement with the explicit DFT results (black curves) [32,33], in particular in the most relevant temperature range for the KWL simulations around 1000 K. Of special importance is the fact that the internal driving force to form a KWL (Fig. 1(e)), which originates from the difference of the two APB energies in combination with the anisotropic factor (cf. Equation (S8)) and which the two available EAM potentials strongly under- or overestimate, is close to DFT for the MTP.

3.2. Formation of KWL

With the optimized MTP, the KWL can be readily created. Fig. 2 documents the formation of an incomplete KWL as observed in an MD simulation at 980 K (without external loading). The corresponding dislocation core configurations are detailed in Section S2 in the Supplementary Materials. In additional test simulations with EAM potentials [48,49], such a spontaneous KWL formation is not observed at similar temperatures.[2]

Snapshots (a) to (c) illustrate the first cross-slip process required to form a KWL. In snapshot (a), the dislocation is initially fully dissociated

---

[1] Numerically, extrapolation by the MTP occurs if the grade is greater than unity. The higher the extrapolation grade, the more severe is the extrapolation by the MTP.

[2] Our calculations show that for the Mishin-EAM [48], a KWL forms for an overheated system at 1200 K and that no KWL formation is feasible for the Du-EAM [49] within the typical MD time scale.
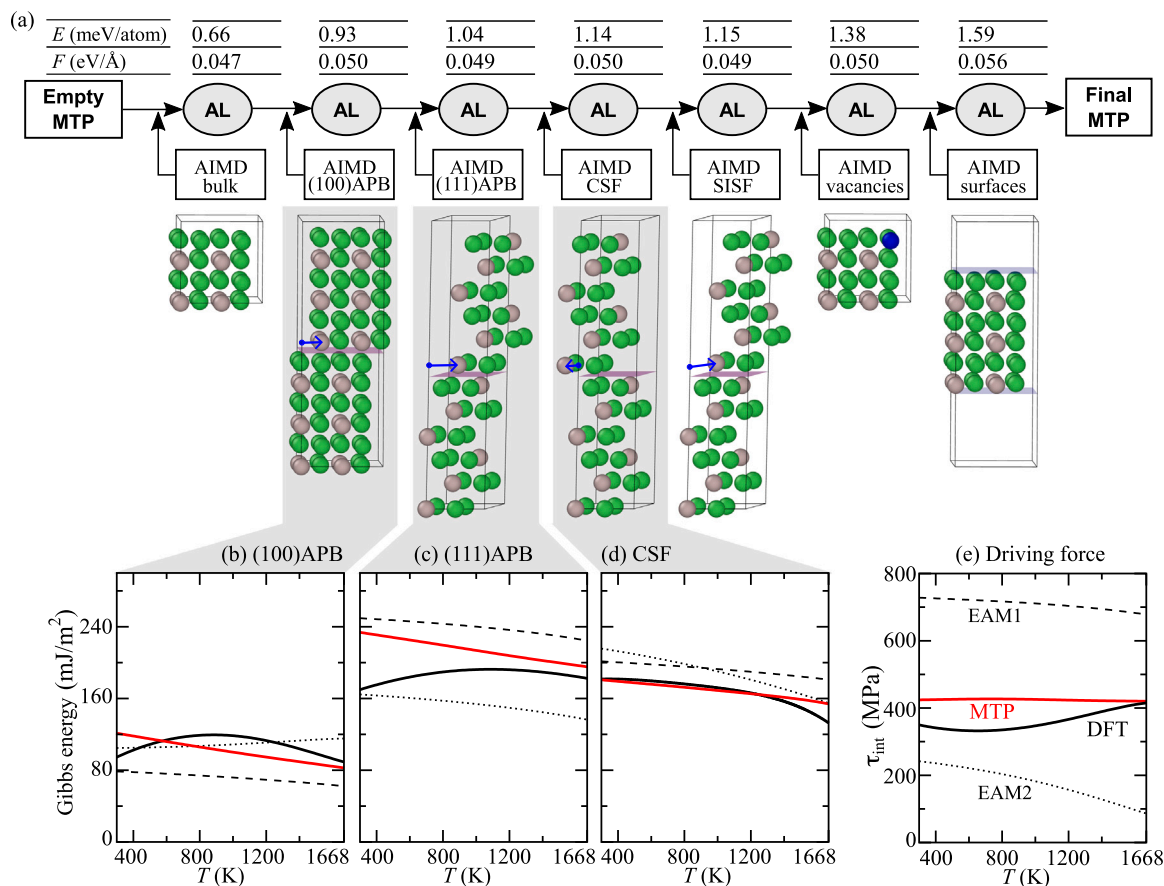
Fig. 1. Machine-learning potential design. (a) Flow diagram of the proposed physically informed active-learning scheme. Every oval labeled "AL" represents a standard active-learning step for the indicated geometry, i.e., bulk structure, (100)APB, (111)APB, CSF, superlattice intrinsic stacking fault (SISF), Ni-vacancy, Al-vacancy, and a surface with its normal along the [100] direction. The atomic structures are simplified for a better illustration. The blue arrows indicate the vectors of the relative shifts needed to generate the planar defects. The input for each subsequent AL-oval is (1) the MTP from the previous AL-step and (2) a set of AIMD configurations for the new geometry to provide basic structural information. The root mean square errors (RMSEs) above each oval represent the fitting errors when completing the respective AL-step. (b)–(d) Temperature-dependent Gibbs formation energies of the planar defects predicted by the *final* MTP. (e) Driving force for the cross-slip process originating from the difference of the two APB energies in combination with the anisotropic factor (cf. Equation (S8) and the related discussion in Supplementary Material). DFT results are from previous works [32,33]. Dashed (EAM1) and dotted (EAM2) curves show results from the EAM potentials modified by Mishin et al. [48] and Du et al. [49], respectively. (For interpretation of the references to color in this figure legend, the reader is referred to the web version of this article.)

on the (111) plane, with each superpartial split into a pair of Shockley partials separated by a CSF ribbon. Then, the lower superpartial cross-slips from the (111) plane to the $(\bar{1}\bar{1}1)$ plane, partially in (b) and fully in (c). At 1234 ps, the second cross-slip of the lower superpartial, from the $(\bar{1}\bar{1}1)$ plane to another (111) plane, is initiated (Fig. 2(d)). When this double cross-slip process is finished, an incomplete KWL has formed (Fig. 2(f)).
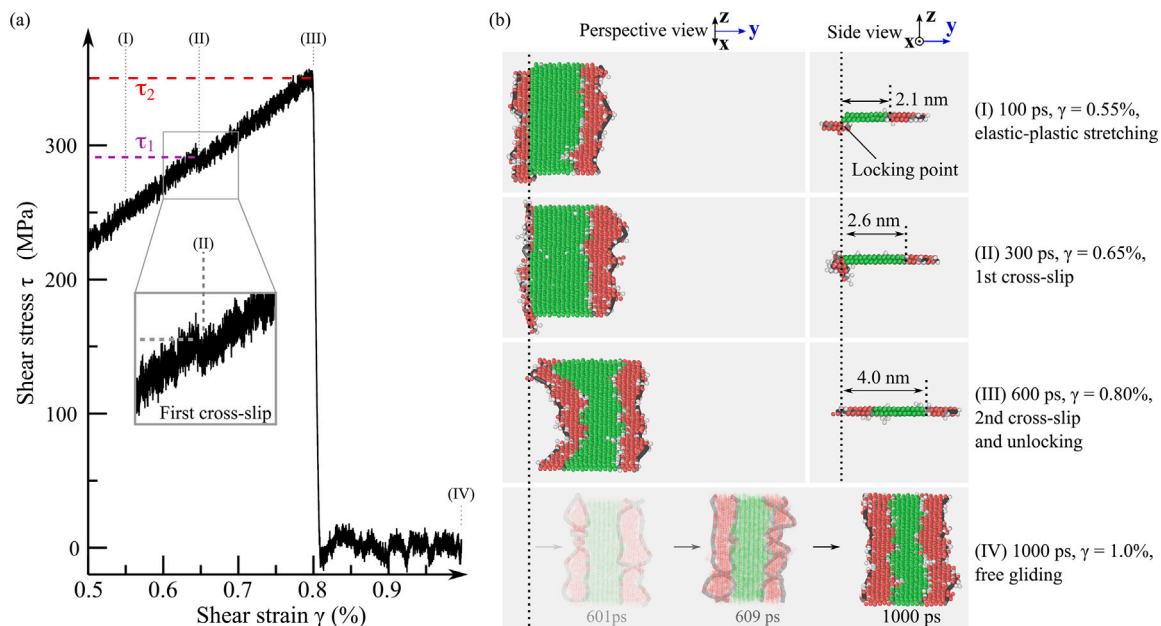
It is worth noting that the distance between the original (111) plane and the (111) plane onto which the superpartial moves during the second cross-slip process is 2δ (see the side view in Fig. 2(d) and (e) and the enlarged front view in Fig. 2(g)), where δ labels the distance between the two nearest atomic planes along the [111] direction. Our results are in agreement with a recent *in situ* scanning tunneling microscopy study [16], which reported 2δ at room temperature and $m\delta$ (with $m \geq 2$) at higher temperatures in Ni$_3$Al (1 at.% Ta), however, without an interpretation. It is the strong internal forces that drive the CSF ribbon in the lower superpartial away from the original (111) plane. An internal torque due to the anisotropic elastic interaction between the two screw superpartials [18,51], indicated in the side view of Fig. 2(b) by the gray arrows, pushes the upper superpartial to the left and the lower superpartial to the right (note that the Burgers vector points out of the paper plane). In the analyzed simulation, the lower superpartial cross-slips first. (The leading and trailing superpartials have the same probability to cross-slip onto a (100) plane, as indicated

by Figure S3 in the Supplementary Materials.) When it is located on the $(\bar{1}\bar{1}1)$ plane, the repulsive force between the two superpartials (cf. double headed arrow in the side view in Fig. 2(d)) drives the lower superpartial to cross-slip again, now to the (111) plane which is 2δ away from the original one. The observed atomistic shape of the cross-slipped segment, specifically the well-defined 2δ distance over the full segment shown in Fig. 2(g), supports the previously suggested "double-jog" mechanism [19]. MD observations show that the jogs are highly mobile and expand rapidly along the dislocation line. Incomplete KWLs with 3δ or 4δ likewise occur in the MD simulations. They form by consecutive cross-slips of both of the superpartials.

The present MD simulations reveal the importance of the superpartial splitting and of the corresponding CSF on the cross-slip behavior. This is a crucial insight since available phenomenological models [17, 19,20] do not explicitly take into account the screw superpartial splitting into Shockley partials. This approximation of considering only *constricted* superpartials favors 1δ-KWL formation at low temperatures and renders 1δ-KWLs to be the intermediate state for forming $m\delta$-KWLs at elevated temperatures. In contrast, the MD simulations show that a 2δ-KWL can form directly without an intermediate 1δ-KWL. We conclude that this is due to the CSF ribbon spanning on the $(\bar{1}\bar{1}1)$ plane. This finding highlights the necessity to carefully consider the effect of the superpartial splitting into Shockley partials and the CSF ribbon on the dislocation behavior.

Fig. 2. Formation of an incomplete KWL at 980 K. Snapshots (a) to (c) display the first cross-slip from a (111) to a $(\bar{1}\bar{1}1)$ plane, and snapshots (d) to (f) the second cross-slip from the $(\bar{1}\bar{1}1)$ plane to another (111) plane. (g) Enlarged dislocation segments at 1234 ps. The dislocation structure is analyzed by using the Dislocation Extraction Algorithm (DXA) in Ovito [50]. Green and red atoms highlight the APB region and the CSF ribbon, respectively. For a clear illustration, atoms not related to the dislocation core structure are removed. The gray tubes highlight Shockley partials, and the blue ones constricted superpartials. (For interpretation of the references to color in this figure legend, the reader is referred to the web version of this article.)

3.3. Unlocking of KWL

The above-discussed KWL with the cross-slip distance of 2δ was sheared at different temperatures T and shear rates $\dot{\gamma}$. The unlocking of the KWL at temperatures $\lesssim 1000$ K involves a two-step cross-slip process in reverse order compared to its formation. Fig. 3 shows a representative stress–strain curve in (a) and selected dislocation structures at critical simulation times in (b).

The shear stress increases with strain at a slope of 45 GPa until point (III) when full unlocking occurs. At the earlier point (II), the trailing superpartial cross-slips from its nesting (111) plane to the $(\bar{1}\bar{1}1)$ plane (difference between the configurations in (I) and (II) in Fig. 3(b)) accompanied by a small stress drop. The second cross-slip of the trailing superpartial from the $(\bar{1}\bar{1}1)$ plane to the (111) glide plane, which hosts the leading superpartial and the APB, happens at point (III) and is followed by a rapid glide of the dislocation (cf. perspective view (IV) in Fig. 3(b)). Accordingly, a stress collapse is observed in the stress–strain curve. After unlocking, the released dislocation either glides freely on the (111) plane or cross-slips to a (100) plane forming a KWL again. The latter occurs in particular at higher temperatures.

An exemplary run at a slightly higher temperature of 1050 K is shown in Fig. 4. Many cross-slip events occur during this simulation and various distinct core configurations of the superdislocation are observed. In addition to the 2δ configuration found for the KWL-formation and unlocking simulation at lower temperatures, here, core configurations can also exist with larger δ values for the superpartials separation, e.g., 3δ (snapshot at 320 ps), 4δ (1580 ps), 5δ (1820 ps), or 6δ (1980 ps). In contrast to the initial KWL-formation, the double cross-slip events at larger separations occur in steps of 1δ, which is a consequence of a smaller driving force. Some of the cross-slip events can be correlated with previous TEM observations [15].

The "APB-jump" observed in *in situ* TEM experiments [15] is replicated on the atomic scale at a shear strain of 1.05%, as illustrated in Fig. 4 in the box labeled "APB-jump". This kind of jump starts from a core structure with two (111)APBs lying connected on two neighboring (111) planes. During the APB-jump, the trailing superpartial cross-slips from the $(\bar{1}\bar{1}1)$ to the lower (111) plane and glides on this (111) plane by a short distance (2.7 nm), which reflects the (111)APB width corresponding to the instantaneous loading state, before cross-slipping to another $(\bar{1}\bar{1}1)$ plane.

Another kind of jump (labeled "dislocation-jump") happens at a slightly higher strain of 1.17%, during which the released dislocation moves shortly freely on the (111) plane but quickly gets stopped due to a cross-slip event. This "dislocation-jump" is, from a broader perspective, similar to the previously observed "long-distance jump" [15] but different in the details of the mechanism proposed in that work. From the MD snapshot at 1400 ps, it is the trailing superpartial that firstly cross-slips to another {111} plane rather than the leading one. A more detailed analysis of the MD simulations shows the mechanism of this "dislocation-jump" to be an inertia effect that asymmetrically impacts the motion of the leading and trailing superpartials. The consequences are asymmetric elastic vibrations of the core structure on the slip plane, different velocities of the leading and trailing superpartial, and eventually, different cross-slip rates. We speculate that this dislocation jump is related to the jerky movement of dislocations in L1$_2$ intermetallics and suggest further research in this direction.

3.4. Temperature-dependent critical stresses

Fig. 5 shows the temperature dependence of the stresses required to unlock a KWL. The lower stress τ_1 corresponds to the first cross-slip of the trailing superpartial. The higher stress τ_2 reflects the highest

Fig. 3. Unlocking of a KWL at $T = 1000$ K and $\dot{\gamma} = 5 \times 10^{-6}$ ps^{-1}. (a) Corresponding stress–strain curve and (b) snapshots at representative times highlighting the evolution of the KWL during unlocking. Snapshot (IV) has only a perspective view. The given times are referenced with respect to the time at the shear strain of $\gamma = 0.5\%$. Atom colors have the same meaning as in Fig. 2. The moving direction is along the y-axis. (For interpretation of the references to color in this figure legend, the reader is referred to the web version of this article.)
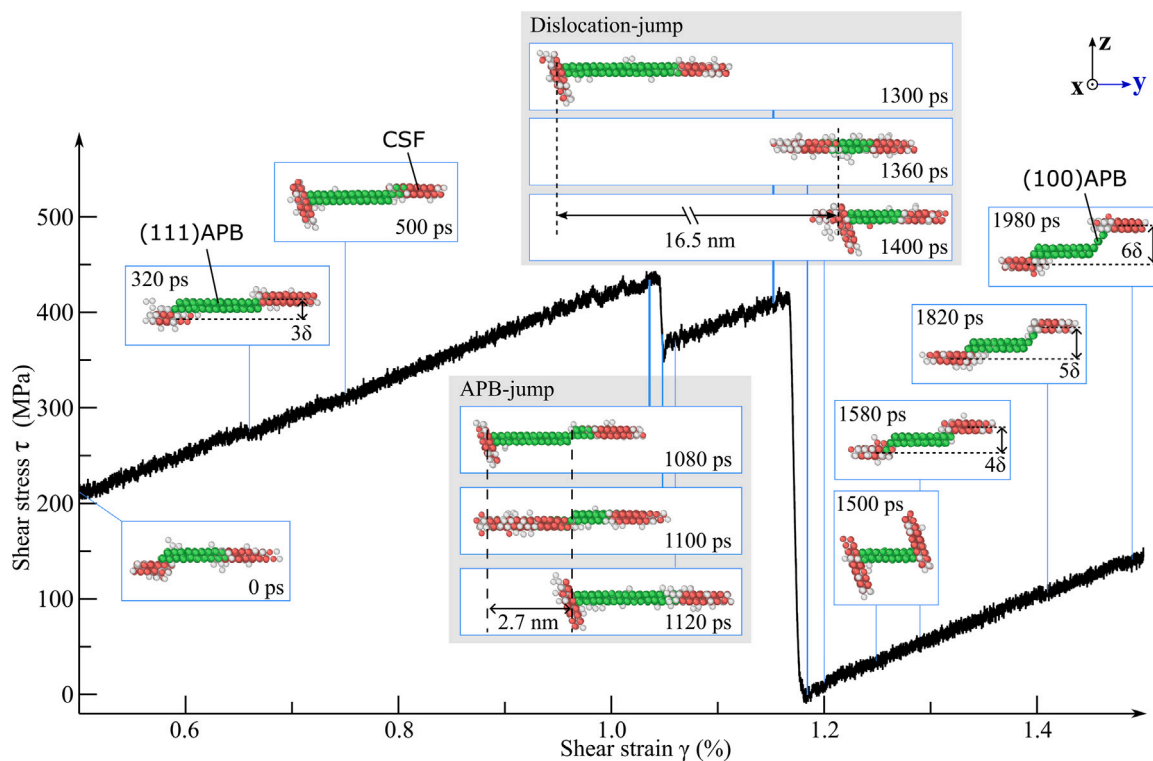
Fig. 4. Unlocking of a KWL at $T = 1050$ K and $\dot{\gamma} = 5 \times 10^{-6}$ ps^{-1}. The given times are referenced with respect to the time at $\gamma = 0.5\%$. Atom colors have the same meaning as in Fig. 2. (For interpretation of the references to color in this figure legend, the reader is referred to the web version of this article.)

stress required to unlock the KWL, which can correspond for example to the second cross-slip of the trailing superpartial or a dislocation jump (cf. discussion in Section 3.3). For both stresses, a strong decrease with temperature is observed. In particular, the unlocking stress τ_2 significantly drops by almost 40% from 568 MPa at 650 K to 351 MPa at 1000 K, suggesting that in the temperature region of YSA, the unlocking of KWLs has a substantial thermal contribution.

Above 1000 K, the two critical stresses exhibit significant statistical fluctuations. Within the available statistics, the averaged τ_1 remains almost unchanged, whereas the unlocking stress τ_2 increases slightly with temperature. The latter is due to the increased cross-slip distances at high temperatures (cf. Fig. 4). In this temperature region, the weak temperature dependence indicates that the thermal component required to constrict the Shockley partials is rather small, and the
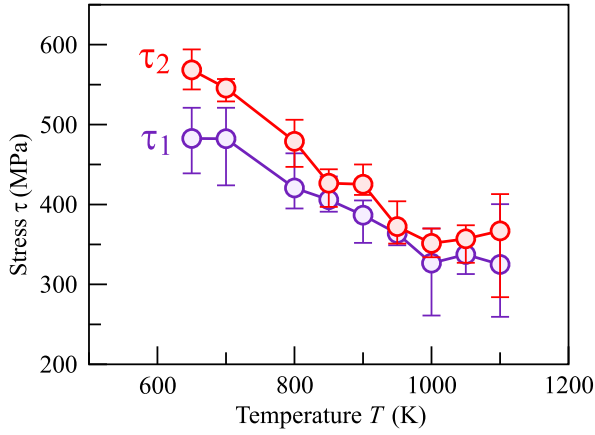
Fig. 5. Temperature-dependent critical stresses at a shear rate of $\dot{\gamma} = 2 \times 10^{-6}$ ps^{-1}. Error bars are determined from three statistical samples. (For interpretation of the references to color in this figure legend, the reader is referred to the web version of this article.)

unlocking process depends mainly on the internal elastic interactions between two superpartials, i.e., the athermal component.

3.5. Phenomenological model

With the atomistically obtained temperature-dependent unlocking stresses, we derive a phenomenological model to predict the unlocking of KWLs, the essence of which is schematically depicted in Fig. 6(a). We decompose the effective stress τ_{eff} required to unlock a KWL into a static component τ_{st} that balances the internal interaction and a thermal component τ^* required to overcome the barrier of the thermally activated unlocking,

$$\tau_{\mathrm{eff}}(T) = \tau_{\mathrm{st}}(T) + \tau^*(T) = \underbrace{\tau_{\mathrm{at}} - \tau_{\mathrm{soft}}(T)}_{\text{static } \tau_{\mathrm{st}}} + \tau^*(T), \tag{7}$$

where, as indicated, τ_{st} is further decomposed into an athermal term τ_{at} and a softening term τ_{soft}. The thermal softening term τ_{soft} accounts for, e.g., the reduced elastic constants at elevated temperatures. The frictional force is implicitly taken into account by fitting to the unlocking stresses.

For a thermally activated process, the energy barrier ΔH can be expressed as [45,52–54]

$$\Delta H = H_0 \left[1 - \left(\frac{\tau^*}{\tau_{0K}^*} \right)^p \right]^q, \tag{8}$$

where H_0 is the enthalpy when τ^* is zero and τ_{0K}^* is the stress to overcome the barrier at 0 K; p and q are activation exponents, for which $p = 0.5$ is widely used for dislocations [22,53,54] and $q = 3/2$ is considered to be general for thermally activated processes [22,55].

The energy barrier ΔH is related to the strain rate $\dot{\gamma}$ via [53,54]

$$\frac{\dot{\gamma}}{\dot{\gamma}_0} = \exp\left(-\frac{\Delta H}{k_{\mathrm{B}}T} \right), \tag{9}$$

with $\dot{\gamma}_0$ a pre-factor and k_{B} the Boltzmann constant. Combining Eqs. (8) and (9), the thermal part τ^* can be written as:

$$\tau^*(T) = \tau_{0K}^* \left[1 - \left(-\frac{k_{\mathrm{B}}T}{H_0} \ln \frac{\dot{\gamma}}{\dot{\gamma}_0} \right)^{2/3} \right]^2. \tag{10}$$

With increasing temperature, the term inside of the square brackets decreases from 1 at $T = 0$ K to 0 at a temperature at which the process is fully activated and which we label T_1. With the assumption of a linear

Table 1
Optimized fitting parameters for the phenomenological model in Eq. (11).

τ_{a} (MPa)	τ_0^* (MPa)	$\dot{\gamma}_0$ (ps^{-1})	H_0 (eV)	ϵ (MPa/K)
463.2	1661.2	4.88×10^{-2}	1.10	0.138

temperature dependence of the thermal softening term, i.e., $\tau_{\mathrm{soft}}(T) = \epsilon \cdot T$, the effective stress reads

$$\tau_{\mathrm{eff}}(T) = \tau_{\mathrm{at}} - \tau_{\mathrm{soft}}(T) + \tau^*(T) = \tau_{\mathrm{at}} - \epsilon \cdot T + \tau_{0K}^* \left[1 - \left(-\frac{k_{\mathrm{B}}T}{H_0} \ln \frac{\dot{\gamma}}{\dot{\gamma}_0} \right)^{2/3} \right]^2, \tag{11}$$

with the thermal term $\tau^*(T)$ cut off at T_1. We fit the unlocking stresses τ_2 obtained from MD simulations at different $\dot{\gamma}$ and T (up to 1000 K) with the derived phenomenological model (Eq. (11)) and obtain the values given in Table 1. The resulting curves for the investigated strain rates are plotted in Fig. 6(b). While the static term τ_{st}, shown as the dashed line labeled "static", demonstrates a slight temperature dependence, the thermally activated term $\tau^*(T)$ represented by the distance between the fitted curve and the "static" line rapidly increases with decreasing temperatures.

4. Discussion

The proposed model, derived from atomistic simulations, can be employed to predict the macroscopic unlocking stress and thereby to achieve a better understanding of the YSA. To this end, the macroscopic process is treated as a collection of microscopic unlocking events of single dislocations, each of which can be described by Eq. (11) with the here obtained parameters (Table 1). This is reasonable because the YSA is known to be mainly caused by cross-slip events that lead to an exhaustion of single, mobile dislocations [16,20,22]. Therefore, the macroscopic unlocking stress can be obtained by substituting the logarithmic term in Eq. (11) with its macroscale counterpart $\ln \left(\dot{\gamma}_{\mathrm{m}}/\dot{\gamma}_{\mathrm{m},0} \right)$, with $\dot{\gamma}_{\mathrm{m}}$ and $\dot{\gamma}_{\mathrm{m},0}$ obtained from Ref. [4] and from Orowan's equation, respectively (see Supplementary Material for details). The resulting temperature-dependent macroscopic unlocking stress is shown in Fig. 6(b) (gray curve). The thermal part of the macroscopic unlocking stress is leftwards shifted, i.e., there is a smaller thermal contribution compared to the microscopic curves due to the longer accessible time frames on the macroscale.

The calculated temperature-dependent macroscopic unlocking stress sheds light on the interpretation of the YSA and the accompanying anomalous work-hardening rate, particularly when it is compared with the measured critical resolved shear stress (CRSS) at 0.2% plastic strain for Ni$_3$Al (black curve) [4], as plotted in Fig. 6(c). Two critical temperatures, T_1 and T_2, are relevant for the formation and the unlocking of KWLs.

Formation of KWLs. The thermally activated component τ^* reduces with increasing temperature and becomes zero at T_1. Along with the decrease of τ^*, the formation of KWLs driven by internal interactions becomes easier due to a reduced cross-slip barrier (without external loading). Therefore, mobile dislocations have a rapidly increasing propensity to get exhausted, resulting in an increase of the dislocation exhaustion rate. This interpretation is in agreement with experimental studies [21,56]. The CRSS and the work-hardening rate $\theta_{0.2}$ (θ at 0.2% plastic strain) increase with temperature. From T_1 onward, a Shockley pair bound by a CSF ribbon can easily constrict and, consequently, most screw dislocations transform into 2δ-KWLs due to the strong internal driving force. Since 2δ-KWLs with constricted superpartials are only metastable, the superpartials further cross-slip along the (100) plane to form $m\delta$-KWLs with $m > 2$ or even complete KWLs, which require higher stresses to unlock. These types of KWLs have been frequently observed in TEM studies at elevated temperatures [57,58]. The CRSS
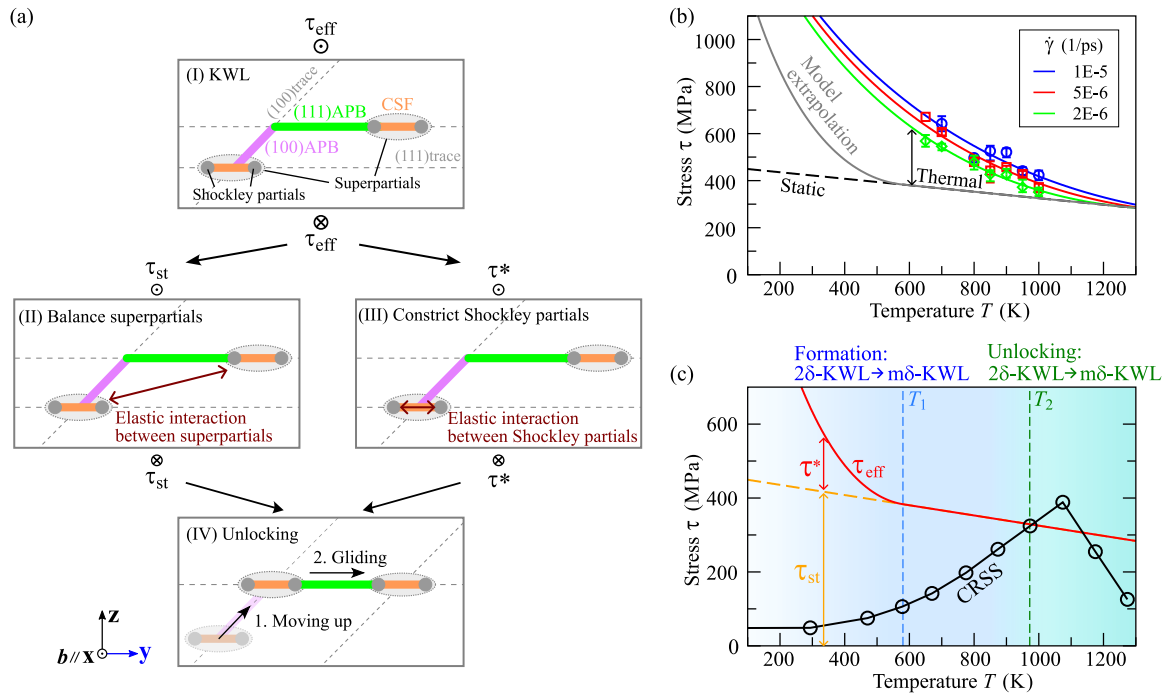
Fig. 6. Phenomenological model describing the evolution of screw superdislocations in L1$_2$ intermetallics. (a) Schematic diagram for the decomposition of the effective stress to unlock a KWL. The applied shear stress points into ($\otimes$) or out of ($\odot$) the page. For simplicity, the lattice friction acting against dislocation movement is neglected in the illustration. (b) Effective stresses fitted to Eq. (11) and the model extrapolation to the macroscale (gray curve). The colored symbols denote values from the MD simulations and the corresponding solid curves represent the model fit at the given shear rates. (c) Comparison between the macroscopic unlocking stress and the critical resolved shear stress (CRSS) (from the 0.2% proof stress) [4]. (For interpretation of the references to color in this figure legend, the reader is referred to the web version of this article.)

and the work-hardening rate $\theta_{0.2}$ increase with temperature at a faster rate.

Unlocking of KWLs. At T_2, the CRSS reaches the stress required to unlock 2δ-KWLs as predicted by the proposed model. The unlocking of 2δ-KWLs suppresses the formation of $m\delta$-KWLs with $m > 2$, thus reducing the exhaustion rate and the work hardening rate $\theta_{0.2}$. The work-hardening rate $\theta_{0.2}$ consequently reaches its maximum around T_2. A similar conclusion was made in Ref. [59] where various experimental measurements were carefully analyzed and in Ref. [60] where the YSA of three L1$_2$ intermetallics with extreme values of planar-defect formation energies was compared. The here obtained $T_2 = 970\,\mathrm{K}$ compares well with the experimentally measured value of 800–850 K at 0.2% plastic strain [56,60]. Upon a further increase of the CRSS, $m\delta$-KWLs with $m > 2$ can be unlocked, and at the critical, maximal value of the CRSS, other gliding mechanisms become active, e.g., gliding on the (100) plane [7] and the APB dragging mechanism [58].

The proposed phenomenological model does not only explain the macroscopic YSA of Ni$_3$Al via the evolution of KWLs, but also clarifies the role of the different planar defects on the YSA by the decomposition into a "static" and a "thermal" component (see Fig. 6). The difference in the two types of APBs contributes mostly to the internal elastic interactions between the superpartials, determining the magnitude of the static component (cf. Equation (S8)). The CSF energy controls the thermally activated constriction of the Shockley partials. Note that the static component turns into the driving force during the formation of KWLs acting against the thermal constriction.

The above discussion and the proposed model can be transferred to understand the yield behavior of other L1$_2$ intermetallics, for example, Co-based intermetallics [9,10] and L1$_2$ strengthened high-entropy alloys [11]. To apply the model, the system-specific model parameters have to be determined. For example, H_0 can be obtained based on the CSF energy and dislocation interactions [61,62]; τ_{at} is given by the APB energies and the elastic anisotropic factor (cf. Equation (S8)); ϵ can be evaluated from the temperature dependence of the elastic constants. With these parameters, T_1 and T_2 are readily available. In addition to

regulating the formation of KWLs, T_1 is also an important factor for determining the activation of gliding systems on {100} planes, as previously pointed out for L1$_2$ intermetallics with high CSF energy [60]. In this respect, the proposed model facilitates the establishment of general constitutive laws for describing the yield behavior of L1$_2$ intermetallics. Tuning YSA for L1$_2$ intermetallics by tailoring the formation energy of planar defects *in silico* is a promising avenue, for example, with the assistance of high-throughput tools [63]. Furthermore, for modeling precipitate-strengthened superalloys that inherit the YSA from their L1$_2$ phase, it is feasible to employ the current model in combination with additional mechanisms, e.g., stacking-fault shearing [64,65].

5. Conclusions

In conclusion, KWLs, the origin of YSA in L1$_2$ intermetallics, can be successfully formed and unlocked *in silico* at the atomistic scale by using an *ab initio*-based and physically informed machine-learning potential. The simulations show a significant temperature dependence of the unlocking stresses, in contrast to previous athermal predictions. To describe the unlocking stresses, we have derived a phenomenological model that integrates both the athermal component and the thermally activated component and that can be extrapolated to the macroscopic scale. By comparing the extrapolated results with experimental values, two critical temperatures have been identified, which are of crucial importance in predicting the evolution of KWLs. The atomistic simulations predict many cross-slip events, some of which reenact experimental observations, such as the direct formation of 2δ-KWLs, the APB-jump, and the dislocation jump. The applicability of the here-acquired knowledge and the phenomenological model to other L1$_2$ intermetallics and, by extension, to L1$_2$-strengthened superalloys has been elaborated.

CRediT authorship contribution statement

Xiang Xu: Writing – review & editing, Writing – original draft, Visualization, Validation, Software, Resources, Methodology, Investigation,

Declaration of competing interest

The authors declare that they have no known competing financial interests or personal relationships that could have appeared to influence the work reported in this paper.

Data availability

The developed MTP, the corresponding DFT training dataset, the atomistic structure of the 2δ-KWL, the thermal properties of L1$_2$ Ni$_3$Al, and the Gibbs energy of the planar defects are openly available on DaRUS (https://doi.org/10.18419/darus-4480).

Appendix A. Supplementary data

Supplementary material related to this article can be found online at https://doi.org/10.1016/j.actamat.2024.120423.

References

[1] T. Pollock, S. Tin, Nickel-based superalloys for advanced turbine engines: chemistry, microstructure and properties, J. Propuls. Power 22 (2) (2006) 361–374, http://dx.doi.org/10.2514/1.18239.

[2] H. Long, S. Mao, Y. Liu, Z. Zhang, X. Han, Microstructural and compositional design of Ni-based single crystalline superalloys — A review, J. Alloys Compd. 743 (2018) 203–220, http://dx.doi.org/10.1016/j.jallcom.2018.01.224.

[3] R.C. Reed, The Superalloys: Fundamentals and Applications, Cambridge University Press, 2008.

[4] D. Golberg, M. Demura, T. Hirano, Effect of Al-rich off-stoichiometry on the yield stress of binary Ni$_3$Al single crystals, Acta Mater. 46 (8) (1998) 2695–2703, http://dx.doi.org/10.1016/S1359-6454(97)00476-X.

[5] S. Takeuchi, E. Kuramoto, Temperature and orientation dependence of the yield stress in Ni$_3$Ga single crystals, Acta Metall. 21 (4) (1973) 415–425, http://dx.doi.org/10.1016/0001-6160(73)90198-3.

[6] N.L. Okamoto, T. Oohashi, H. Adachi, K. Kishida, H. Inui, P. Veyssière, Plastic deformation of polycrystals of Co$_3$ (Al, W) with the L1$_2$ structure, Phil. Mag. 91 (28) (2011) 3667–3684, http://dx.doi.org/10.1080/14786435.2011.586158.

[7] Y.M. Wang-Koh, Understanding the yield behaviour of L1$_2$-ordered alloys, Mater. Sci. Technol. 33 (8) (2017) 934–943, http://dx.doi.org/10.1080/02670836.2016.1215961.

[8] Y. Eggeler, K. Vamsi, T. Pollock, Precipitate shearing, fault energies, and solute segregation to planar faults in Ni-, CoNi-, and Co-base superalloys, Annu. Rev. Mater. Res. 51 (2021) 209–240, http://dx.doi.org/10.1146/annurev-matsci-102419-011433.

[9] A. Suzuki, H. Inui, T. Pollock, L1$_2$-strengthened cobalt-base superalloys, Annu. Rev. Mater. Res. 45 (2015) 345–368, http://dx.doi.org/10.1146/annurev-matsci-070214-021043.

[10] Z. Chen, K. Kishida, H. Inui, M. Heilmaier, U. Glatzel, G. Eggeler, Improving the intermediate-and high-temperature strength of L1$_2$-Co$_3$ (Al, W) by Ni and Ta additions, Acta Mater. 238 (2022) 118224, http://dx.doi.org/10.1016/j.actamat.2022.118224.

[11] B.X. Cao, H.J. Kong, Z.Y. Ding, S.W. Wu, J.H. Luan, Z.B. Jiao, J. Lu, C.T. Liu, T. Yang, A novel L1$_2$-strengthened multicomponent Co-rich high-entropy alloy with both high γ'-solvus temperature and superior high-temperature strength, Scr. Mater. 199 (2021) 113826, http://dx.doi.org/10.1103/PhysRevB.50.17953.

[12] T. Yang, Y. Zhao, W. Liu, J. Kai, C. Liu, L1$_2$-strengthened high-entropy alloys for advanced structural applications, J. Mater. Res. 33 (19) (2018) 2983–2997, http://dx.doi.org/10.1557/jmr.2018.186.

[13] P. Veyssière, J. Douin, P. Beauchamp, On the presence of super lattice intrinsic stacking faults in plastically deformed Ni$_3$Al, Phil. Mag. A 51 (3) (1985) 469–483, http://dx.doi.org/10.1080/01418618508237567.

[14] Y.Q. Sun, P.M. Hazzledine, A TEM weak-beam study of dislocations in γ' in a deformed Ni-based superalloy, Phil. Mag. A 58 (4) (1988) 603–617, http://dx.doi.org/10.1080/01418618808209940.

[15] G. Molenat, D. Caillard, Dislocation mechanisms in Ni$_3$Al at room temperature, in situ straining experiments in TEM, Phil. Mag. A 64 (6) (1991) 1291–1317, http://dx.doi.org/10.1080/01418619108225350.

[16] C. Coupeau, J. Michel, J. Bonneville, M. Drouet, An atomic-scale insight into Ni$_3$Al slip traces, Materialia 9 (2020) 100563, http://dx.doi.org/10.1016/j.mtla.2019.100563.

[17] V. Paidar, D.P. Pope, V. Vitek, A theory of the anomalous yield behavior in L1$_2$ ordered alloys, Acta Metall. 32 (3) (1984) 435–448, http://dx.doi.org/10.1016/0001-6160(84)90117-2.

[18] M.H. Yoo, On the theory of anomalous yield behavior of Ni$_3$Al–Effect of elastic anisotropy, Scr. Metall. (U. S.) 20 (6) (1986) http://dx.doi.org/10.1016/0036-9748(86)90466-7.

[19] P.B. Hirsch, A new theory of the anomalous yield stress in L1$_2$ alloys, Phil. Mag. A 65 (3) (1992) 569–612, http://dx.doi.org/10.1080/01418619208201539.

[20] D. Caillard, V. Paidar, A model for the anomalous mechanical properties of nickel-base L1$_2$ ordered alloys—I. Dislocations dynamics, Acta Mater. 44 (7) (1996) 2759–2771, http://dx.doi.org/10.1016/1359-6454(95)00388-6.

[21] T. Kruml, E. Conforto, B. Lo. Piccolo, D. Caillard, J.L. Martin, From dislocation cores to strength and work-hardening: a study of binary Ni$_3$Al, Acta Mater. 50 (20) (2002) 5091–5101, http://dx.doi.org/10.1016/S1359-6454(02)00364-6.

[22] Y.S. Choi, D.M. Dimiduk, M.D. Uchic, T.A. Parthasarathy, Modelling plasticity of Ni$_3$Al-based L1$_2$ intermetallic single crystals, I. Anomalous temperature dependence of the flow behaviour, Phil. Mag. 87 (12) (2007) 1939–1965, http://dx.doi.org/10.1080/14786430601169782.

[23] M. Demura, D. Golberg, T. Hirano, An athermal deformation model of the yield stress anomaly in Ni$_3$Al, Intermetallics 15 (10) (2007) 1322–1331, http://dx.doi.org/10.1016/j.intermet.2007.04.007.

[24] M.H. Yoo, M.S. Daw, M.I. Baskes, Atomistic simulation of superdislocation dissociation in Ni$_3$Al, At. Simul. Mater.: Beyond Pair Potentials (1989) 401–410, http://dx.doi.org/10.1007/978-1-4684-5703-2.

[25] M. Wen, D.L. Lin, Effect of elastic center on dislocation core structure in ni3al, Acta Mater. 45 (3) (1997) 1005–1008, http://dx.doi.org/10.1016/S1359-6454(96)00229-7.

[26] T. Parthasarathy, D. Dimiduk, Atomistic simulations of the structure and stability of PPV locks in an L1$_2$ compound, Acta Mater. 44 (6) (1996) 2237–2247, http://dx.doi.org/10.1016/1359-6454(95)00362-2.

[27] A.H.W. Ngan, M. Wen, C.H. Woo, Atomistic simulations of Paidar–Pope–Vitek lock formation in Ni$_3$Al, Comput. Mater. Sci. 29 (3) (2004) 259–269, http://dx.doi.org/10.1016/j.commatsci.2003.10.003.

[28] S. Rao, D. Dimiduk, T. Parthasarathy, M. Uchic, C. Woodward, Atomistic simulations of intersection cross-slip nucleation in L1$_2$ Ni$_3$Al, Scr. Mater. 66 (6) (2012) 410–413, http://dx.doi.org/10.1016/j.scriptamat.2011.12.002.

[29] M. Wakeda, T. Osada, T. Ohmura, Atomistic analysis of temperature-dependent dislocation dynamics in Ni$_3$Al-based intermetallic alloys, Mater. Today Commun. 37 (2023) 106987, http://dx.doi.org/10.1016/j.mtcomm.2023.106987.

[30] A.V. Shapeev, Moment tensor potentials: A class of systematically improvable interatomic potentials, Multiscale Model. Simul. 14 (3) (2016) 1153–1173, http://dx.doi.org/10.1137/15M1054183.

[31] K. Gubaev, E.V. Podryabinkin, G.L.W. Hart, A.V. Shapeev, Accelerating high-throughput searches for new alloys with active learning of interatomic potentials, Comput. Mater. Sci. 156 (2019) 148–156, http://dx.doi.org/10.1016/j.commatsci.2018.09.031.

[32] X. Xu, X. Zhang, A. Ruban, S. Schmauder, B. Grabowski, Strong impact of spin fluctuations on the antiphase boundaries of weak itinerant ferromagnetic Ni$_3$Al, Acta Mater. 255 (2023) 118986, http://dx.doi.org/10.1016/j.actamat.2023.118986.

[33] X. Xu, X. Zhang, A. Ruban, S. Schmauder, B. Grabowski, Accurate complex-stacking-fault gibbs energy in Ni₃Al at high temperatures, Scr. Mater. 242 (2024) 115934, http://dx.doi.org/10.1016/j.scriptamat.2023.115934.

[34] I.S. Novikov, K. Gubaev, E.V. Podryabinkin, A.V. Shapeev, The mlip package: moment tensor potentials with MPI and active learning, Mach. Learn.: Sci. Technol. 2 (2) (2020) 025002, Website: 10.1088/2632-2153/abc9fe.

[35] G. Kresse, J. Hafner, Ab initio molecular dynamics for liquid metals, Phys. Rev. B 47 (1993) 558–561, http://dx.doi.org/10.1103/PhysRevB.47.558.

[36] G. Kresse, J. Hafner, Ab initio molecular-dynamics simulation of the liquid-metal–amorphous-semiconductor transition in germanium, Phys. Rev. B 49 (1994) 14251–14269, http://dx.doi.org/10.1103/PhysRevB.49.14251.

[37] P.E. Blöchl, Projector augmented-wave method, Phys. Rev. B 50 (24) (1994) 17953, http://dx.doi.org/10.1103/PhysRevB.50.17953.

[38] J.P. Perdew, K. Burke, M. Ernzerhof, Generalized gradient approximation made simple, Phys. Rev. Lett. 77 (1996) 3865–3868, http://dx.doi.org/10.1103/PhysRevLett.77.3865.

[39] A. Togo, I. Tanaka, First principles phonon calculations in materials science, Scr. Mater. 108 (2015) 1–5, http://dx.doi.org/10.1016/j.scriptamat.2015.07.021.

[40] P. Hirel, Atomsk: A tool for manipulating and converting atomic data files, Comput. Phys. Comm. 197 (2015) 212–219, Website: 10.1016/j.cpc.2015.07.012.

[41] P.M. Anderson, J.P. Hirth, J. Lothe, Theory of Dislocations, Cambridge University Press, 2017.

[42] A.P. Thompson, H.M. Aktulga, R. Berger, D.S. Bolintineanu, M. Brown, P. Crozier, P. in't Veld, A. Kohlmeyer, S. Moore, T. Nguyen, et al., LAMMPS-a flexible simulation tool for particle-based materials modeling at the atomic, meso, and continuum scales, Comput. Phys. Comm. 271 (2022) 108171, Website: 10.1016/j.cpc.2021.108171.

[43] D. Rodney, Activation enthalpy for kink-pair nucleation on dislocations: Comparison between static and dynamic atomic-scale simulations, Phys. Rev. B 76 (14) (2007) 144108, http://dx.doi.org/10.1103/PhysRevB.76.144108.

[44] T. Lee, J. Qi, C.A. Gadre, H. Huyan, S.T. Ko, Y.X. Zuo, C.J. Du, J. Li, T. Aoki, R.Q. Wu, et al., Atomic-scale origin of the low grain-boundary resistance in perovskite solid electrolyte Li₀.₃₇₅Sr₀.₄₃₇₅Ta₀.₇₅Zr₀.₂₅O₃, Nature Commun. 14 (1) (2023) 1940, http://dx.doi.org/10.1038/s41467-023-37115-6.

[45] S. Yin, Y. Zuo, A. Abu-Odeh, H. Zheng, X.G. Li, J. Ding, S.P. Ong, M. Asta, R.O. Ritchie, Atomistic simulations of dislocation mobility in refractory high-entropy alloys and the effect of chemical short-range order, Nat. Commun. 12 (1) (2021) 4873, http://dx.doi.org/10.1038/s41467-021-25134-0.

[46] L. Erhard, J. Rohrer, K. Albe, V. Deringer, Modelling atomic and nanoscale structure in the silicon–oxygen system through active machine learning, Nature Commun. 15 (1) (2024) 1927, http://dx.doi.org/10.1038/s41467-024-45840-9.

[47] L. Mismetti, M. Hodapp, Automated atomistic simulations of dissociated dislocations with ab initio accuracy, Phys. Rev. B 109 (9) (2024) 094120, http://dx.doi.org/10.1103/PhysRevB.109.094120.

[48] Y. Mishin, Atomistic modeling of the γ and γ'-phases of the Ni–Al system, Acta Mater. 52 (6) (2004) 1451–1467, http://dx.doi.org/10.1016/j.actamat.2003.11.026.

[49] J.P. Du, C.Y. Wang, T. Yu, Construction and application of multi-element EAM potential (Ni–Al–Re) in γ/γ' Ni-based single crystal superalloys, Modelling Simul. Mater. Sci. Eng. 21 (1) (2012) 015007, http://dx.doi.org/10.1088/0965-0393/21/1/015007.

[50] A. Stukowski, K. Albe, Extracting dislocations and non-dislocation crystal defects from atomistic simulation data, Modelling Simul. Mater. Sci. Eng. 18 (8) (2010) 085001, Website: 10.1088/0965-0393/18/8/085001.

[51] M.H. Yoo, Stability of superdislocations and shear faults in L1₂ ordered alloys, Acta Metall. 35 (7) (1987) 1559–1569, http://dx.doi.org/10.1016/0001-6160(87)90102-7.

[52] U. Kocks, A. Argon, M. Ashby, Thermodynamics and kinetics of slip, 1975.

[53] S. Nemat-Nasser, W. Guo, Flow stress of commercially pure niobium over a broad range of temperatures and strain rates, Mater. Sci. Eng. A 284 (1–2) (2000) 202–210, http://dx.doi.org/10.1016/S0921-5093(00)00740-1.

[54] N. Zotov, B. Grabowski, Molecular dynamics simulations of screw dislocation mobility in bcc Nb, Modelling Simul. Mater. Sci. Eng. 29 (8) (2021) 085007, http://dx.doi.org/10.1088/1361-651X/ac2b02.

[55] J. Li, The mechanics and physics of defect nucleation, MRS Bull. 32 (2) (2007) 151–159, http://dx.doi.org/10.1557/mrs2007.48.

[56] J. Bonneville, J.L. Martin, P. Spätig, B. Viguier, B. Matterstock, Mechanical properties of binary Ni₃Al single crystals, MRS Online Proc. Libr. (OPL) 460 (1996) http://dx.doi.org/10.1557/PROC-460-419.

[57] H.P. Karnthaler, E. Th. Mühlbacher, C. Rentenberger, The influence of the fault energies on the anomalous mechanical behaviour of Ni₃Al alloys, Acta Mater. 44 (2) (1996) 547–560, http://dx.doi.org/10.1016/1359-6454(95)00191-3.

[58] C. Rentenberger, H. Karnthaler, On the origin of work softening of Ni₃Al deformed along [001] above the peak temperature, Mater. Sci. Eng. A 319 (2001) 347–351, http://dx.doi.org/10.1016/S0921-5093(01)01022-X.

[59] T. Kruml, J.L. Martin, B. Viguier, J. Bonneville, P. Spätig, Deformation microstructures in Ni₃(Al, Hf), Mater. Sci. Eng.: A 239 (1997) 174–179, http://dx.doi.org/10.1016/S0921-5093(97)00578-9.

[60] E. Conforto, G. Molénat, D. Caillard, Comparison of Ni-based alloys with extreme values of antiphase boundary energies: dislocation mechanisms and mechanical properties, Phil. Mag. 85 (2–3) (2005) 117–137, http://dx.doi.org/10.1080/14786430412331315626.

[61] X.X. Yu, C.Y. Wang, Effect of alloying element on dislocation cross-slip in γ'-Ni₃Al: a first-principles study, Phil. Mag. 92 (32) (2012) 4028–4039, http://dx.doi.org/10.1080/14786435.2012.700419.

[62] K. Vamsi, S. Karthikeyan, Yield anomaly in L1₂ Co₃AlₓW₁₋ₓ vis-à-vis Ni₃Al, Scr. Mater. 130 (2017) 269–273, http://dx.doi.org/10.1016/j.scriptamat.2016.11.039.

[63] K. Vamsi, S. Karthikeyan, High-throughput estimation of planar fault energies in A₃B compounds with L1₂ structure, Acta Mater. 145 (2018) 532–542, http://dx.doi.org/10.1016/j.actamat.2017.10.029.

[64] Y. Wang-Koh, O. Messe, C. Schwalbe, C. Jones, C. Rae, The effect of strain rate on the tensile deformation behavior of single crystal, Ni-based superalloys, Metall. Mater. Trans. A 54 (5) (2023) 1456–1468, http://dx.doi.org/10.1007/s11661-023-07007-x.

[65] A. Parsa, M. Sirrenberg, D. Bürger, M. Mills, A. Dlouhy, G. Eggeler, Yield stress anomaly and creep of single crystal Ni-base superalloys–Role of particle size, Mater. Sci. Eng. A 899 (2024) 146403, http://dx.doi.org/10.1016/j.msea.2024.146403.